Internal Tide Surface Signature and Incoherence in the North Atlantic

Noé Lahaye, Aurélien Ponte, Julien Le Sommer, Aurélie Albert

AGU ADVANCING EARTH AND SPACE SCIENCES

Geophysical Research Letters

RESEARCH LETTER
10.1029/2024GL108508

Internal Tide Surface Signature and Incoherence in the North Atlantic

Noé Lahaye[1], Aurélien Ponte[2], Julien Le Sommer[3], and Aurélie Albert[3]

[1]Odyssey Team, Inria & IRMAR, Campus Universitaire de Beaulieu, Rennes, France, [2]Laboratoire d'Océanographie Physique et Spatiale, Ifremer, Université de Brest, CNRS, IRD, IUEM, Brest, France, [3]University Grenoble Alpes, CNRS UMR IGE, Grenoble, France

Key Points:

- Surface signatures of semidiurnal coherent and incoherent internal tides are quantified and decomposed into vertical mode contributions
- Intra-annual decorrelation time scale is typically less than 20 days for the first baroclinic mode, and less than 10 days for higher modes
- Mean levels of incoherence of sea level and current are 55% and 68% (variance fraction), reflecting a larger high mode content in currents

Supporting Information:

Supporting Information may be found in the online version of this article.

Correspondence to:

N. Lahaye,
noe.lahaye@inria.fr

Citation:

Lahaye, N., Ponte, A., Le Sommer, J., & Albert, A. (2024). Internal tide surface signature and incoherence in the North Atlantic. *Geophysical Research Letters*, *51*, e2024GL108508. https://doi.org/10.1029/2024GL108508

Received 25 JAN 2024
Accepted 3 MAY 2024

Author Contributions:

Conceptualization: Noé Lahaye, Aurélien Ponte
Data curation: Noé Lahaye, Aurélie Albert
Formal analysis: Noé Lahaye, Aurélien Ponte
Funding acquisition: Julien Le Sommer
Investigation: Noé Lahaye
Methodology: Noé Lahaye, Aurélien Ponte
Resources: Julien Le Sommer, Aurélie Albert
Software: Noé Lahaye, Aurélien Ponte, Aurélie Albert
Validation: Noé Lahaye, Julien Le Sommer, Aurélie Albert
Visualization: Noé Lahaye
Writing – original draft: Noé Lahaye

Abstract Despite intensified efforts to better quantify Internal Tide dynamics over past decades, large uncertainties remain regarding their distribution and lifecycle in the ocean. In particular, internal tide incoherence (loss of time-regularity) has limited our ability to characterize, understand, and predict internal tides, challenging the exploitation of new-generation wide-swath satellite altimeters. Based on a realistic high-resolution numerical simulation, we quantify the internal tide distribution and incoherence properties in the North Atlantic. We quantify IT incoherence for sea level and surface currents, and for different vertical modes independently. Our results show that typical decorrelation timescale induced by the mesoscale turbulence are rather short—below 25 days for the first vertical mode. It further exhibits a strong dependence of the internal tide incoherence with location, reflecting regions of enhanced eddy activity, and with vertical mode number—higher baroclinic modes being much more incoherent with shorter decorrelation timescale.

Plain Language Summary Internal tides are perturbations of currents and density that propagate in the ocean (i.e., internal waves) and are generated when the astronomical tide flows over underwater topographic features. Because of interactions with other types of currents in the ocean, the corresponding signal is not perfectly regular in time, which has limited our understanding and ability to predict these motions for decades. In this study, we quantify this loss-of-regularity of the internal tides based on a numerical simulation of the North Atlantic.

1. Introduction

Internal Tides (IT) are an important part of ocean dynamics with first order impact on ocean mixing, the ocean global circulation and the transport of biogeochemical species (e.g., Ferrari & Wunsch, 2009; Whalen et al., 2020). Because of its strong signature, in particular on the surface horizontal currents and Sea Level Anomaly (SLA), IT have a footprint in remote sensing or in situ observations (Arbic et al., 2015; Hennon et al., 2019). This is of crucial importance in the context of next generation wide-swath satellite altimeters—including the most recent SWOT mission (Morrow et al., 2019) –, as they aim at mapping of ocean currents at the near-submesoscale (<100 km) where the spatial signature of balanced motions and IT overlap (Torres et al., 2019). This observational issue has urged the need for a better characterization and mapping capability of IT in order to remove the corresponding signal from the observations. At the same time, and with more direct implication for the physical oceanography community, these observational efforts represent a unique opportunity to improve our understanding of internal tides dynamics and their role in the ocean. This context fostered the development of new methods for estimating the internal tide from new-era observational data, some of them including a physical model through some data-assimilation strategies (e.g., Carrère et al., 2021; Le Guillou et al., 2021, and see references therein).

It is well known that a substantial fraction of IT is incoherent, that is, IT do not solely consist of a set of harmonic constituents at the astronomical tide frequencies. This incoherence results from interactions with lower frequency (mesoscale) variability (e.g., Kunze, 1985; Rainville & Pinkel, 2006; Zaron & Egbert, 2014), and was identified decades ago in frequency spectra from tidal gauges time series, where it appears in the form of "cusps" centered around the tidal frequency peaks (e.g., Munk et al., 1965; Munk & Cartwright, 1966; Colosi & Munk, 2006). It has been extensively studied ever since, and recent estimates, based on satellite altimeter data (Zaron, 2017), ARGO parking-phase data (Geoffroy & Nycander, 2022) or realistic numerical simulations (Nelson et al., 2019), have shown that more than a half of the internal tide variance could be incoherent. Estimates of typical decorrelation

Writing – review & editing: Noé Lahaye, Aurélien Ponte, Julien Le Sommer, Aurélie Albert

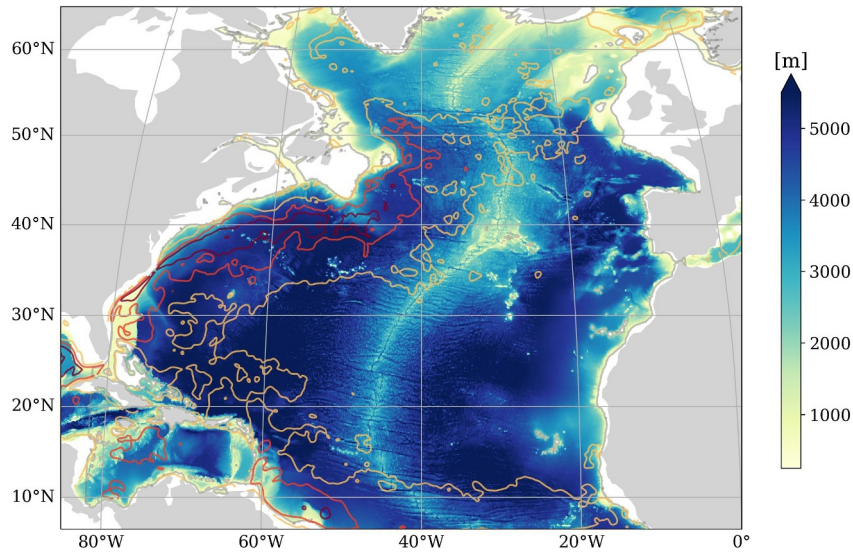

Figure 1. Topography used in the eNATL60 simulation (the domain shown is restricted to the region analyzed in the paper, which is smaller than the full numerical domain). Regions masked for the analysis are delimited by a gray contour (regions shallower than 250 m appear white). The RMS amplitude of mesoscale surface currents (computed as the square root of EKE, where the latter is based on the low-pass filtered surface current with a cutoff period of 2 days) is superimposed with light orange, dark orange and dark red contours at 15, 30, and 45 cm/s.

timescales have yield values down to 30 days, sometimes shorter, in addition to a clear signature of seasonality (Buijsman et al., 2017; Geoffroy & Nycander, 2022; Zaron, 2022) and in agreement with in situ observations (e.g., Nash et al., 2012; van Haren, 2004; Zilberman et al., 2011). IT incoherence is a major obstacle for IT mapping from altimetric data, essentially because it is based on harmonic analysis to de-alias the high-frequency tidal signal from multi-day repeat satellite altimeter data.

Despite the above-mentioned advances on the subject, the lifecycle and incoherence of internal tides remain insufficiently well constrained and call for further effort. In this paper, we characterize the surface signature of internal tides in the North Atlantic Ocean using the high-resolution realistic numerical simulation eNATL60 (Brodeau et al., 2020; Uchida et al., 2022). One key aspect of our results relies on a vertical mode decomposition of the IT fields, enabling a meaningful decomposition of the IT signature, and from which we estimate and discuss incoherence levels as well as typical time of loss-of-coherence.

2. Material and Methods

We used hourly outputs from the high-resolution realistic numerical simulation of the North Atlantic eNATL60 (Brodeau et al., 2020). The domain of investigation, with the corresponding bathymetry, is shown in Figure 1. eNATL60 uses the ocean numerical model NEMO (Madec et al., 2019) with an horizontal resolution of 1/60° (around 1.5 km at mid-latitude) and 300 vertical levels, with atmospheric forcing from the ERA-Interim reanalysis, barotropic tidal forcing including the frequency components M_2, S_2, N_2, K_1 and 0_1, and the corresponding barotropic tide signal imposed at the open boundaries of the domain using FES2014 (Lyard et al., 2020). More details on the simulation, as well as validation material, can be found in Brodeau et al. (2020) and Uchida et al. (2022), and in Supporting Information S1. While the simulation, after a spinup phase, is more than 1 year long (from 2009/06/30 to 2010/10/29), this study includes only the first 8 months (due to technical limitations), and regions that are deeper than 250 m. The Mediterranean sea and the Gulf of Mexico (west of 82°W) are further discarded from the analysis.

We analyzed the surface fields (Sea Level Anomaly—SLA—and horizontal currents) and further performed a vertical mode decomposition of the pressure and horizontal velocity. This decomposition was achieved by projecting the pressure p and horizontal velocity (u, v) on vertical eigenmodes given by the standard Sturm-Liouville problem for hydrostatic internal waves (e.g. Gill, 1982, chap. 6), which were computed using a stratification profile obtained from the time-averaged temperature and density field. More details on the procedure can

be found in Bella et al. (2024), and the corresponding python codes are available online (https://github.com/NoeLahaye/ITideNATL). The modal contribution at the surface can then be computed from modal amplitudes (projection coefficient for a given field) and the surface value of the vertical modes. We focus on the first 3 to 4 modes (including the barotropic one) in this paper. One can estimate the summed contribution from higher modes by subtracting the surface contribution of these low modes to surface fields. Along the same line, the RMS reduction of the residual baroclinic signal above a mode number K can be computed as follows:

$$\sigma_K^{(f)} = \sqrt{\left\langle \left| f - \sum_{n=1}^{K} f_n \right|^2 \right\rangle / \langle |f|^2 \rangle}, \tag{1}$$

where f denote the baroclinic surface contribution of a given field and f_n is the surface signature of mode n.

Let us mention that in the limit of horizontal plane wave solution (and horizontally homogeneous background), indicated by a hat below, one can derive polarization relations for the projected fields (e.g., Kelly et al., 2021) and obtain the following relation:

$$|\hat{u}_n|^2 + |\hat{v}_n|^2 = \frac{\omega^2 + f^2}{\omega^2 - f^2} \frac{|\hat{p}_n|^2}{{c_n}^2}, \tag{2}$$

where c_n is the mode n eigenvalue (horizontal phase speed). This indicates that pressure perturbations relative to the currents fluctuations vanish at the critical latitude where $f \to \omega$ (74.5° for M_2), and that the relative magnitude of currents compared to pressure increases with the mode number (since c_n decreases with n).

From time series of surface fields and modal amplitudes, the semi-diurnal internal tide signal was extracted using a complex demodulation at the semidiurnal frequency. For any time series $f_{\mathrm{tot}}(t)$, the internal tide component in the semi-diurnal band can be expressed as $f(t) = \Re\left[\tilde{f}(t)e^{i\omega_c t}\right]$, where ω_c is the semidiurnal frequency ($2\pi/\omega_c = 12.2$ hr) In this expression, $\tilde{f}(t)$ is a slowly varying complex amplitude, whose variability encompasses both interference between different tidal constituents and the demodulation frequency, and the incoherent part of the signal. Complex demodulation gives access to this amplitude by computing:

$$\tilde{f} = 2\mathcal{L}_{\mathrm{LP}}\left[f_{\mathrm{tot}}(t)e^{-i\omega_c t}\right],$$

where $\mathcal{L}_{\mathrm{LP}}$ denotes a low-pass filter whose cut-off frequency is directly linked to the band-with of an equivalent band-pass filter. We used a 4th order Butterworth filter with an inverse cut-off frequency of 2 days (equivalent bandwidth of 0.5 cpd). The choice of cut-off frequency is not without consequences, as different bandwidth can lead to different estimates of decorrelation timescale (e.g., Zaron, 2022), the broader, the shorter, while a broad bandwidth exposes to contamination by non-wave motions. We used a fairly broad bandwidth, taking advantage of the fact that vertical mode decomposition enhances the separation between internal tides and non-wave motions (Torres et al., 2022).

The coherent part was simply extracted by fitting complex harmonics to the complex-demodulated time series:

$$\tilde{f}^{(C)} = \sum_k \tilde{f}_k e^{i(\omega_k - \omega_c)t},$$

to obtain the amplitudes $\tilde{f}_k$ of the coherent tide (here, $k \in (M_2, S_2, N_2)$, the semidiurnal constituents included in the potential in the numerical simulations). The incoherent signal is thus defined as the residual:

$$\tilde{f}^{(I)} = \tilde{f} - \tilde{f}^{(C)}.$$

from which we estimated the relative incoherent modal energy fraction $R_n^{(I)}$ as follows:

$$R_n^{(I)} = \frac{|\tilde{p}_n^{(I)}|^2/c_n^2 + |\tilde{u}_n^{(I)}|^2 + |\tilde{v}_n^{(I)}|^2}{|\tilde{p}_n|^2/{c_n}^2 + |\tilde{u}_n|^2 + |\tilde{v}_n|^2}.$$

Finally, the autocorrelation of the incoherent tide time series, given by

$$C(\tau) = \int \overline{\tilde{f}^{(I)}}(t)\tilde{f}^{(I)}(t+\tau)dt$$

(where $\bar{\cdot}$ denotes complex conjugate), was computed over 30-day time windows. Note that the autocorrelation $C(\tau)$ is complex valued, although its imaginary part vanishes at $\tau = 0$ ($C(0)$ is the variance). Hence, prior to this computation, we removed from $\tilde{f}^{(I)}(t)$ a constant phase drift, which reflects the difference between the chosen demodulation frequency and the actual central (mean) frequency. This detrending allows to keep the imaginary part of $C(\tau)$ smaller than the real part. We then fit the autocorrelation using a simple exponentially decaying model:

$$C(\tau)^{\text{fit}} = Ae^{-\tau/T_{\text{inc}}}, \tag{3}$$

where the real-valued parameters, A and T_{inc}, correspond to the variance and the decorrelation time, respectively. This approach is inspired from recent analyses based on observations or numerical simulations (Caspar-Cohen et al., 2022; Geoffroy & Nycander, 2022; Zaron, 2015).

Some aspects of the methodology described above should be further commented. The coherent tide is defined over a duration of 8 months in this study, which is shorter that what other have used—in particular for altimetric data, where time windows of a few years (up to 20 years or so) are commonly used (e.g., Carrère et al., 2021; Zaron, 2019). Furthermore, the estimation of the decorrelation time scale is based on 30 days time windows, and the model (3) includes a single timescale, while several timescales could be expected (for instance, Zaron (2022) reported typical decorrelation time of 180 and 30 days). Here, we focus on incoherence time scales typical of mesoscale features, leaving aside loss of coherence over longer time periods that are associated with different dynamical features in the ocean, such as seasonality or inter-annual variability (see Ansong et al., 2015, their Figure 8).

3. Results

3.1. Characterization of the Surface Signature of IT Across Scales

We first discuss the sea level and surface current signature of the semidiurnal internal tides on a per vertical mode basis, shown in Figure 2. Note that each vertical mode is approximately associated with a typical horizontal wavelength through the corresponding local eigenvalue (Gill, 1982).

As expected, one can identify on all maps main known IT generation sites as amplitude maxima (from West to East and South to North): the Caribbean islands, two seamounts localized around 10°N along the mid-Atlantic Ridge, Cape Verde, Georges Bank, the Azores Islands and the seamounts South of it, and the Bay of Biscay. In addition, intense horizontal kinetic energy is observed at Rockall Trough and in the South Norwegian Basin (limited by the upper boundary of the numerical domain). The first baroclinic mode clearly stands as the dominant contribution to SLA, while higher modes are relatively more important for surface currents. This is expected from the polarization relation (2), and we checked that this relation—which is strictly valid for horizontal plane wave—holds qualitatively by comparing the corresponding maps of modal variance (not shown). Averaged over the domain of analysis, the RMS amplitude associated with the first baroclinic modes accounts for 47% of the total for the SLA, while it reaches only 25% for the surface currents. For the latter, modes three and higher collectively have a slightly greater contribution than the first two modes, accounting for 54% of the total variability on average. Higher modes exhibit a broader spatial distribution, as they are generated by smaller topographic features that are more evenly distributed—for example, along mid-ocean ridges—while low baroclinic modes are predominantly generated by steep isolated features of large amplitudes (e.g., Vic et al., 2018; Garrett & Kunze, 2007).

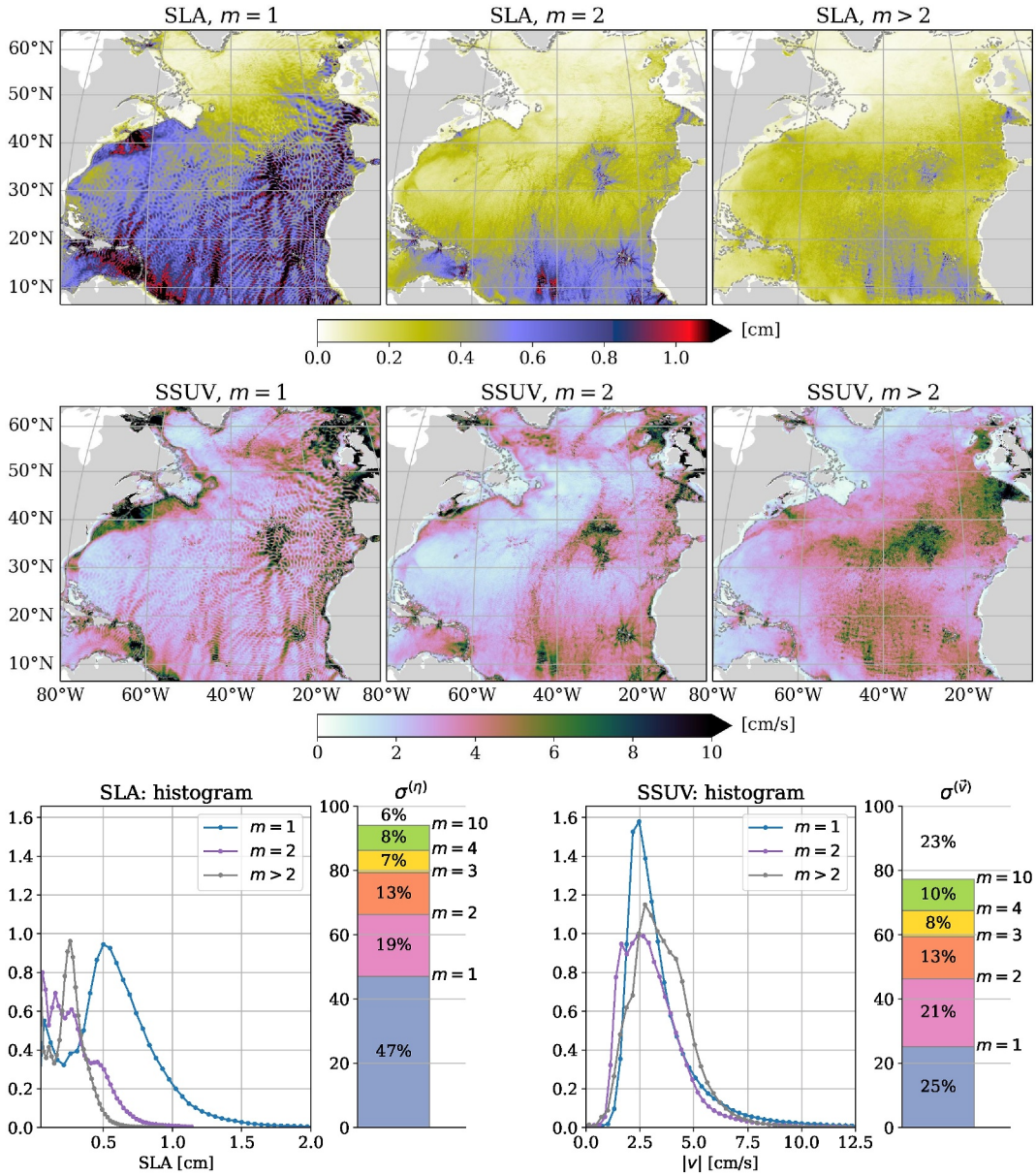

Figure 2. RMS modal contribution for Sea Level Anomaly (first row) and surface horizontal currents (second row). First baroclinic (left column), second baroclinic (right column) and baroclinic residual (right columns) are shown. The corresponding histograms are shown in the lower row (left: SLA, right: horizontal currents) as well as the relative modal contribution (stacked bar plots, following Equation 1).

The amplitude of the SLA signature decreases with latitude, while the opposite holds for surface currents, which is in agreement with the polarization relations (2). A potential implication is that while IT might be hard to quantify from altimeter data at high latitude, it can still have a strong signature on the horizontal currents, which calls for complementary methods or observations—such as surface drifters—to estimate the corresponding variability.

3.2. Quantification of Internal Tide Incoherence

We now address more specifically internal tide incoherence, looking at the incoherent energy fraction (per vertical mode) and decorrelation timescale of the incoherent part. As visible in Figure 3 (upper two rows), there is —globally—an increase of the incoherent fraction with mode number, especially between mode 1 and mode 2. Indeed, the mean incoherent energy fraction (weighted by total modal energy) is 38% for the mode 1 in the deep

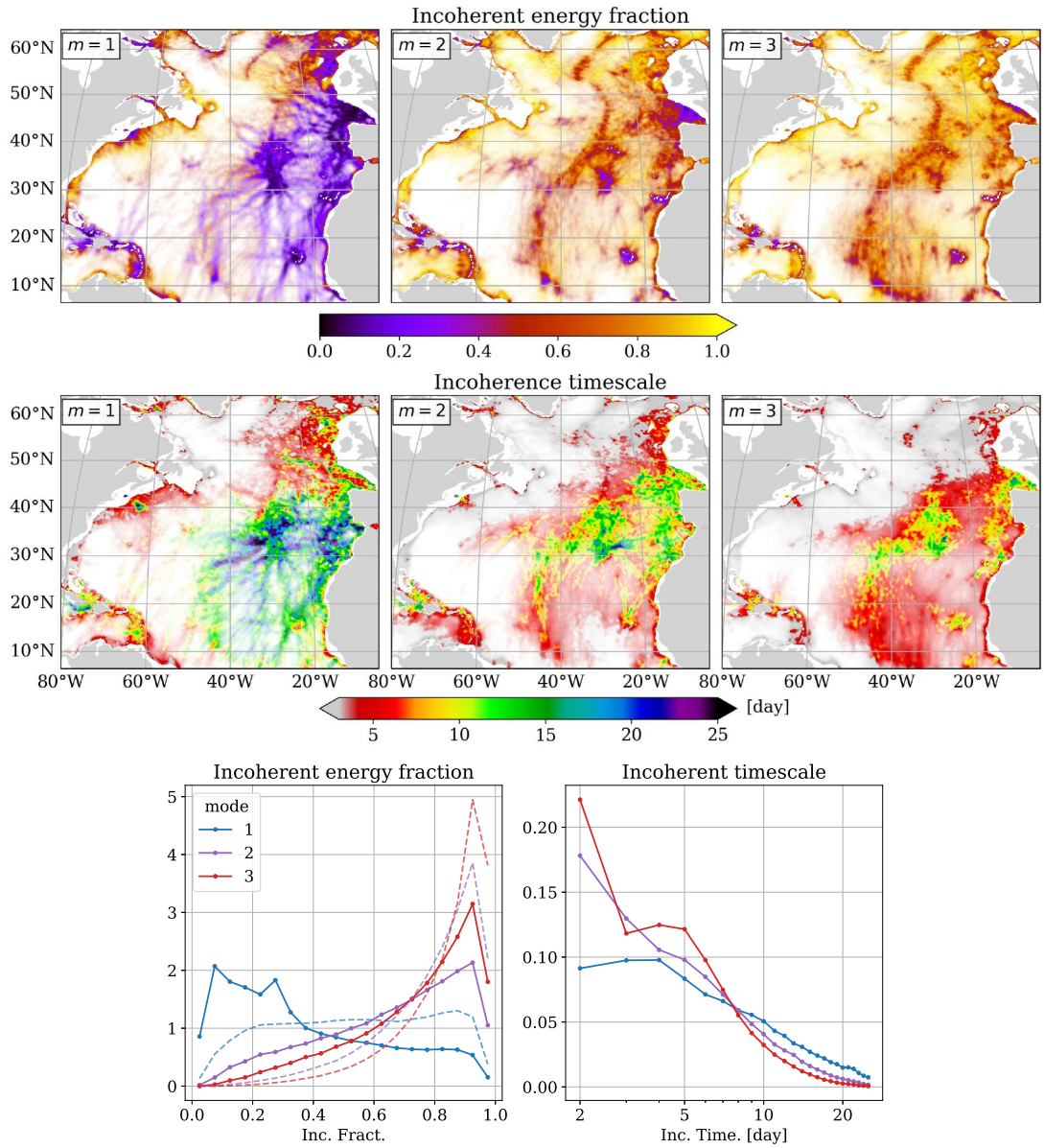

Figure 3. Incoherent energy fraction $R_n^{(I)}$ (upper row) and incoherence timescale (middle row) for the vertical modes 1 (left column) to 3 (right column). For visualization purpose, fields are spatially smoothed (Gaussian Kernel with width 3 km). Furthermore, plots are shaded by the relative magnitude of the square root of the modal energy density (also smoothed in space), as regions of very weak internal tide signal tend to be highly incoherent. Distribution of these estimates (weighted by the modal energy density) are also shown in the bottom row (continuous lines with dots indicating the center of bins), and the dashed lines in the lower left panel corresponds to the unweighted distributions.

ocean and goes up to 66% and 74% for modes 2 and 3 (respective unweighted values are 54%, 78%, and 84%). The decorrelation timescale exhibits, qualitatively, patterns that are similar to the incoherent fraction (the higher the incoherent fraction, the shorter the decorrelation timescale), and thereby a similar dependence with respect to space and mode number. The weighted mean incoherence timescale is 9.3 days for $m = 1$, 6.8 days for $m = 2$ and 5.8 days for $m = 3$. The first three modes have similar incoherence timescale distribution (Figure 3, bottom right panel), although there are more occurrences of long incoherence timescale (>10 days) for mode 1 than higher modes. Notice that the strong peak in the distribution for the bin 2–3 days corresponds to the limit of the lowpass filter used for the complex demodulation, but indicates incoherence timescale that could be shorter than 2 days.

Let us discuss the geographical characterization of IT incoherence. We find that low incoherence fraction (down to 10% in energy for $m = 1$) with longer incoherence timescale (up to 25 days for the $m = 1$) are mainly observed nearby major generation sites and in regions of weak mesoscale activity (cf. Figure 1), for example, onto and East of the Mid-Atlantic Ridge. Conversely, the western part of the basin exhibit strongly incoherent tide with timescales of order 5 days (for $m = 1$) away from the generation site. Notice the loss of coherence that is clearly visible as the beam emanating off the Gulf of Maine interacts with the Gulf Stream, near 65°W, 40°N, which agrees with previous studies (Duda et al., 2018; Kelly et al., 2016; Kelly & Lermusiaux, 2016). Interestingly, the observed timescales are relatively short near the continental shelves, especially along the American coast and in the Northern part of the domain (above 50°N). This corroborates previous studies (e.g., Nash et al., 2012, and references therein) and could be associated with interactions with coastal processes.

We find that regions of weak activity have a predominantly incoherent signal. Indeed, the distribution of incoherent energy fraction (Figure 3, lower row) exhibits less incoherence when weighted by the modal energy (e.g., mode 1 is predominantly incoherent in the unweighted distribution but becomes predominantly coherent in the weighted distribution). In these regions, the IT field is fed by waves that have been scattered from their average trajectory by balanced (mesoscale) currents (and, conversely, this horizontal scattering weakens the coherent IT). Hence, the resulting IT field is mostly incoherent.

3.3. IT Incoherence: Sea Level Anomaly Versus Surface Currents

We end the results section addressing the implication of internal tide incoherence to its observability. To this aim, we look at the distribution of the *reduced* internal tide complex amplitude, defined as the ratio of the complex amplitude of the full IT signal divided by the complex amplitude of the coherent component $\tilde{f}/\tilde{f}^{(C)}$. This quantity indicates how incoherent is the IT signature at a given instant and location (and is equal to 1 when $\tilde{f} = \tilde{f}^{(C)}$). The distribution of the reduced IT is computed after normalization by the RMS amplitude (with respect to time), either within spatial bins of size 30 km—for further estimating the space variability of this distribution—or over the full domain of analysis. These estimates (Figure 4) indicate that incoherence consists of perturbations of both the amplitude and phase of IT. Focusing on the modal distributions (Figure 4, right panels), one sees that the bin-wise interquatile range is fairly narrow (especially for the amplitude, not so much for the phase for $m = 1$), indicating that these distributions are fairly representative of the entire North-Atlantic basin. (Let us mention that the distribution of the raw IT modal complex amplitude can be retrieved from the reduced distribution by rescaling the amplitude by $1/\sqrt{1 - R_n^{(I)}}$.) The spread of the distributions increase for increasing mode number (Figure 4, right panels). Furthermore, the distribution of phase anomaly, albeit peaked around 0, shows that opposite phase can be observed, all the more so for $m > 1$.

As mentioned previously, surface currents have a greater contribution from higher modes (see Section 3.1) than Sea Level Anomaly. At the same time, higher modes are more incoherent (see Figures 2 and 3, right panel). As a result, one can expect that baroclinic horizontal surface currents are more incoherent than the baroclinic sea level fluctuations. This is indeed what we observe: the (weighted) mean incoherent variance fraction is higher for currents—68%—than for SLA—55% (corresponding maps are shown in Figure S3 in Supporting Information S1). Furthermore, baroclinic surface currents (Figure 4, lower left panel) exhibit a distribution with more spread: the fraction of *mostly coherent* (defined as $|1 - \tilde{f}/\tilde{f}^{(C)}| < 0.5$) IT signature is 27% for SLA and decreases to 20% for the surface currents. We checked that these results are in agreement with linear theory. Indeed, we found that the relative contribution of each mode to surface currents versus SLA is well captured by the linear polarization relation (2), and that averaging the incoherent energy fraction (Figure 3, upper panels) weighted by the relative modal contribution reconstructs the SLA and surface current incoherent variance fraction within a good agreement: the weighted mean values as reported above are 63% for horizontal currents and 53% for SLA, when estimated in this way.

4. Conclusions

This paper reports on an analysis of the sea surface signature of the semidiurnal internal tide in the high-resolution numerical simulation of the North Atlantic Ocean eNATL60, and a detailed characterization of its incoherence. Our results show that loss-of-coherence of IT mostly occurs over time scales below 20 days with some variations (down to 2 days) that reflects major generation sites and mesoscale activity. For high vertical modes ($m > 1$), the

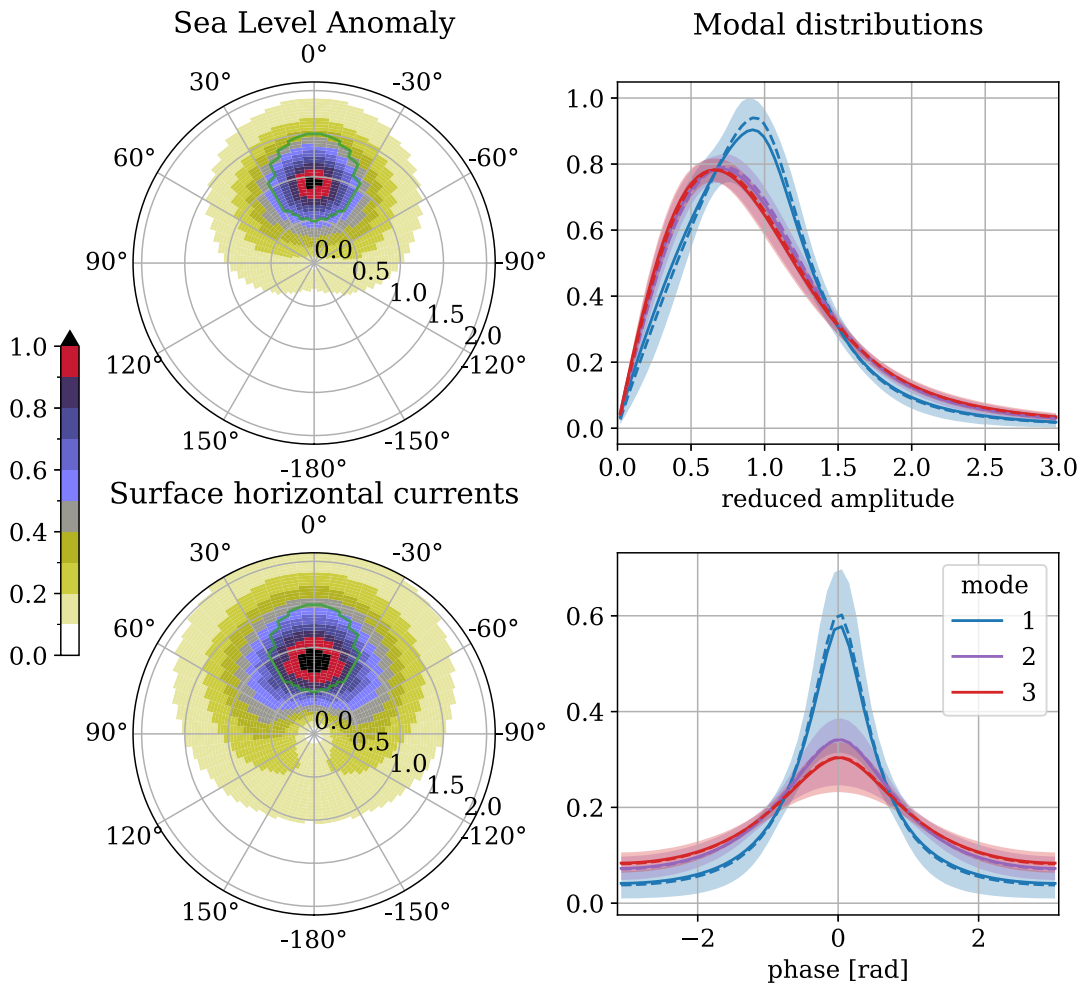

Figure 4. Distribution of the reduced IT surface signature. Left column: Phase/amplitude space-time distribution of the full baroclinic Sea Level Anomaly (top) and horizontal currents (bottom). Region with $|\tilde{f}/\tilde{f}^{(C)} - 1| \leq 0.5$ is marked out by a green contour, and the histograms are normalized by the value of the bin with unit reduced amplitude and zero phase anomaly (which corresponds to the coherent signal). Right column: distribution of the reduced amplitude (top) and phase anomaly (bottom) for the first three vertical mode (the distribution of modal SLA and horizontal currents, which are very similar, have been averaged). The interquatile range (bin-wise) is filled with the color used for plotting the spatial mean distribution (solid line), where individual distributions are computed over horizontal bins of width 30 km. In addition, the space-time histogram computed over the whole domain and time period, weighted by the RMS amplitude, is shown in dashed lines. Each time series is normalized by its RMS amplitude before computing the histograms.

incoherent fraction accounts for much more than half of the total energy with decorrelation timescale below 15 days and down to ~2 days, except in the close vicinity of the generation sites. Furthermore, while the characteristics per vertical mode are very similar for the induced Sea Level Anomaly and surface horizontal currents, the latter have a higher content of high vertical modes which, combined with their higher degree of incoherence, implies that IT surface currents are more incoherent than Sea Level Anomaly (68% vs. 55% in terms of mean incoherent variance fraction).

These results can be discussed in the context of altimeter observations, and in particular of the SWOT mission launched in December 2022. To this aim, we can infer a decorrelation lengthscale from the decorrelation timescale T_{inc}, multiplying it by the typical group velocity of each vertical mode, and compare these estimates with the typical revisit time and distance between consecutive track (21 days and 150 km for SWOT). The typical mode 1 group velocity roughly ranges between 1 and 3 m/s. Thus, the decorrelation lengthscale associated with an incoherence timescale of 10 days is between 860 and 2,600 km. Shorter decorrelation timescales, and especially for higher vertical modes which have a smaller group velocity (the group velocity roughly scales like the inverse mode number) will have a much shorter typical decorrelation lengthscale, down to a few hundreds of km (e.g.,

400 km for $C_g = 1$ m/s and $T_{inc} = 5$ days), indicating that statistically based inverse method are unlikely to be able to reconstruct a significant part of the incoherent tide from altimeter data. These considerations support that using a model of the internal tide accounting for interactions with the mesoscale, as proposed by Kelly et al. (2021) and Le Guillou et al. (2021) may be key to circumvent these limitations.

Data Availability Statement

The material and source files describing the eNATL60 simulation are available at Brodeau et al. (2020). The data and notebook used for processing the Figures in the paper, as well as a python library used for processing the eNATL60 outputs, are available at Lahaye (2024). The library can also be found at https://github.com/NoeLahaye/ITideNATL. The data set used for comparison of the semidiurnal variability with surface drifters estimate in the Supplementary Information is available at Caspar-Cohen (2024).

Acknowledgments
N. Lahaye acknowledges support from the French research funding agency under the ModITO project (ANR-22-CE01-0006-01). N. Lahaye and A. Ponte had support from the TOSCA-ROSES SWOT project DIEGO, and J. Le Sommer and A. Albert from the TOSCA-ROSES SWOT project MIDAS. Computing resources for the analysis of eNATL60 data model have been provided by CINES supercomputing center (Montpellier, France) through GENCI.

References

Ansong, J. K., Arbic, B. K., Buijsman, M. C., Richman, J. G., Shriver, J. F., & Wallcraft, A. J. (2015). Indirect evidence for substantial damping of low-mode internal tides in the open ocean. *Journal of Geophysical Research: Oceans*, *120*(9), 6057–6071. https://doi.org/10.1002/2015jc010998

Arbic, B. K., Lyard, F., Ponte, A., Ray, R. D., Richman, J. G., Shriver, J. F., et al. (2015). Tides and the SWOT mission: Transition from science definition team to science team. *Civil and Environmental Engineering Faculty Publications and Presentations*, *10*. Retrieved from http://archives.pdx.edu/ds/psu/16710

Bella, A., Lahaye, N., & Tissot, G. (2024). Internal tides energy transfers and interactions with the mesoscale circulation in two contrasted areas of the North Atlantic. In B. Chapron, D. Crisan, D. Holm, E. Mémin, & A. Radomska (Eds.), *Stochastic Transport in Upper Ocean Dynamics II* (pp. 1–16). Springer Nature Switzerland. https://doi.org/10.1007/978-3-031-40094-0_1

Brodeau, L., Le Sommer, J., & Albert, A. (2020). ocean-next/eNATL60: Material describing the set-up and the assessment of NEMO-eNATL60 simulations [Dataset]. *Zenodo*. https://doi.org/10.5281/zenodo.4032732

Buijsman, M. C., Arbic, B. K., Richman, J. G., Shriver, J. F., Wallcraft, A. J., & Zamudio, L. (2017). Semidiurnal internal tide incoherence in the equatorial Pacific. *Journal of Geophysical Research: Oceans*, *122*, 5286–5305. https://doi.org/10.1002/2016JC012590

Carrère, L., Arbic, B. K., Dushaw, B., Egbert, G., Erofeeva, S., Lyard, F., et al. (2021). Accuracy assessment of global internal-tide models using satellite altimetry. *Ocean Science*, *17*(1), 147–180. https://doi.org/10.5194/os-17-147-2021

Caspar-Cohen, Z. (2024). Surface drifters and high resolution global simulations mapping of internal tide surface energy [Dataset]. *Zenodo*. https://doi.org/10.5281/zenodo.10851200

Caspar-Cohen, Z., Ponte, A., Lahaye, N., Carton, X., Yu, X., & Gentil, S. L. (2022). Characterization of internal tide incoherence: Eulerian versus Lagrangian perspectives. *Journal of Physical Oceanography*, *52*(6), 1245–1259. https://doi.org/10.1175/JPO-D-21-0088.1

Colosi, J. A., & Munk, W. (2006). Tales of the venerable Honolulu tide gauge. *Journal of Physical Oceanography*, *36*(6), 967–996. https://doi.org/10.1175/JPO2876.1

Duda, T. F., Lin, Y.-T., Buijsman, M., & Newhall, A. E. (2018). Internal tidal modal ray refraction and energy ducting in baroclinic gulf stream currents. *Journal of Physical Oceanography*, *48*(9), 1969–1993. https://doi.org/10.1175/JPO-D-18-0031.1

Ferrari, R., & Wunsch, C. (2009). Ocean circulation kinetic energy: Reservoirs, sources, and sinks. *Annual Review of Fluid Mechanics*, *41*(1), 253–282. https://doi.org/10.1146/annurev.fluid.40.111406.102139

Garrett, C., & Kunze, E. (2007). Internal tide generation in the deep ocean. *Annual Review of Fluid Mechanics*, *39*(1), 57–87. https://doi.org/10.1146/annurev.fluid.39.050905.110227

Geoffroy, G., & Nycander, J. (2022). Global mapping of the nonstationary semidiurnal internal tide using Argo data. *Journal of Geophysical Research: Oceans*, *127*(4). https://doi.org/10.1029/2021JC018283

Gill, A. E. (1982). In *Atmosphere-Ocean dynamics* (Vol. 30). Academic Press.

Hennon, T. D., Alford, M. H., & Zhao, Z. (2019). Global assessment of semidiurnal internal tide aliasing in Argo profiles. *Journal of Physical Oceanography*, *49*(10), 2523–2533. https://doi.org/10.1175/JPO-D-19-0121.1

Kelly, S. M., & Lermusiaux, P. F. J. (2016). Internal-tide interactions with the gulf stream and middle Atlantic bight shelfbreak front. *Journal of Geophysical Research: Oceans*, *121*(8), 6271–6294. https://doi.org/10.1002/2016JC011639

Kelly, S. M., Lermusiaux, P. F. J., Duda, T. F., & Haley, P. J. (2016). A Coupled-mode shallow-water model for tidal analysis: Internal tide reflection and refraction by the gulf stream. *Journal of Physical Oceanography*, *46*(12), 3661–3679. https://doi.org/10.1175/JPO-D-16-0018.1

Kelly, S. M., Waterhouse, A. F., & Savage, A. C. (2021). Global dynamics of the stationary M2 Mode-1 internal tide. *Geophysical Research Letters*, *48*(11), e2020GL091692. https://doi.org/10.1029/2020GL091692

Kunze, E. (1985). Near-inertial wave propagation in geostrophic shear. *Journal of Physical Oceanography*, *15*(5), 544–565. https://doi.org/10.1175/1520-0485(1985)015⟨0544:NIWPIG⟩2.0.CO;2

Lahaye, N. (2024). Material supporting the article "Internal tide surface signature and incoherence in the North Atlantic" by Lahaye et al (GRL, 2024) [Dataset]. *Zenodo*. https://doi.org/10.5281/zenodo.11109622

Le Guillou, F., Lahaye, N., Ubelmann, C., Metref, S., Cosme, E., Ponte, A., et al. (2021). Joint estimation of balanced motions and internal tides from future wide-swath altimetry. *Journal of Advances in Modeling Earth Systems*, *13*(12), e2021MS002613. https://doi.org/10.1029/2021MS002613

Lyard, F. H., Allain, D. J., Cancet, M., Carrère, L., & Picot, N. (2020). FES2014 global ocean tides atlas: Design and performances. *Ocean Science Discussions*. https://doi.org/10.5194/os-2020-96

Madec, G., Bourdallé-Badie, R., Chanut, J., Clementi, E., Coward, A., Ethé, C., et al. (2019). NEMO ocean engine. https://doi.org/10.5281/ZENODO.1464816

Morrow, R., Fu, L.-L., Ardhuin, F., Benkiran, M., Chapron, B., Cosme, E., et al. (2019). Global observations of fine-scale ocean surface topography with the surface water and ocean topography (SWOT) mission. *Frontiers in Marine Science*, *6*, 232. https://doi.org/10.3389/fmars.2019.00232

Munk, W. H., & Cartwright, D. E. (1966). Tidal spectroscopy and prediction. *Philosophical Transactions of the Royal Society A*, *259*(1105), 533–581. https://doi.org/10.1098/rsta.1966.0024

Munk, W. H., Zetler, B., & Groves, G. W. (1965). Tidal cusps. *Geophysical Journal International*, *10*(2), 211–219. https://doi.org/10.1111/j.1365-246X.1965.tb03062.x

Nash, J., Shroyer, E., Kelly, S., Inall, M., Duda, T., Levine, M., et al. (2012). Are any coastal internal tides predictable? *Oceanography*, *25*(2), 80–95. https://doi.org/10.5670/oceanog.2012.44

Nelson, A. D., Arbic, B. K., Zaron, E. D., Savage, A. C., Richman, J. G., Buijsman, M. C., & Shriver, J. F. (2019). Toward realistic nonstationarity of semidiurnal baroclinic tides in a hydrodynamic model. *Journal of Geophysical Research: Oceans*, *124*(9), 6632–6642. https://doi.org/10.1029/2018JC014737

Rainville, L., & Pinkel, R. (2006). Propagation of low-mode internal waves through the ocean. *Journal of Physical Oceanography*, *36*(6), 1220–1236. https://doi.org/10.1175/JPO2889.1

Torres, H. S., Klein, P., D'Asaro, E., Wang, J., Thompson, A. F., Siegelman, L., et al. (2022). Separating energetic internal gravity waves and small-scale frontal dynamics. *Geophysical Research Letters*, *49*(6), e2021GL096249. https://doi.org/10.1029/2021GL096249

Torres, H. S., Klein, P., Siegelman, L., Qiu, B., Chen, S., Ubelmann, C., et al. (2019). Diagnosing ocean-wave-turbulence interactions from space. *Geophysical Research Letters*, *46*(15), 2019GL083675. https://doi.org/10.1029/2019GL083675

Uchida, T., Le Sommer, J., Stern, C., Abernathey, R. P., Holdgraf, C., Albert, A., et al. (2022). Cloud-based framework for inter-comparing submesoscale-permitting realistic ocean models. *Geoscientific Model Development*, *15*(14), 5829–5856. https://doi.org/10.5194/gmd-15-5829-2022

van Haren, H. (2004). Incoherent internal tidal currents in the deep ocean. *Ocean Dynamics*, *54*(1), 66–76. https://doi.org/10.1007/s10236-003-0083-2

Vic, C., Naveira Garabato, A. C., Green, J. A. M., Spingys, C., Forryan, A., Zhao, Z., & Sharples, J. (2018). The lifecycle of semidiurnal internal tides over the northern mid-Atlantic ridge. *Journal of Physical Oceanography*, *48*(1), 61–80. https://doi.org/10.1175/JPO-D-17-0121.1

Whalen, C. B., de Lavergne, C., Naveira Garabato, A. C., Klymak, J. M., MacKinnon, J. A., & Sheen, K. L. (2020). Internal wave-driven mixing: Governing processes and consequences for climate. *Nature Reviews Earth & Environment*, *1*(11), 606–621. https://doi.org/10.1038/s43017-020-0097-z

Zaron, E. D. (2015). Nonstationary internal tides observed using dual-satellite altimetry. *Journal of Physical Oceanography*, *45*(9), 2239–2246. https://doi.org/10.1175/JPO-D-15-0020.1

Zaron, E. D. (2017). Mapping the nonstationary internal tide with satellite altimetry. *Journal of Geophysical Research: Oceans*, *122*(1), 539–554. https://doi.org/10.1002/2016JC012487

Zaron, E. D. (2019). Baroclinic tidal sea level from exact-repeat mission altimetry. *Journal of Physical Oceanography*, *49*(1), 193–210. https://doi.org/10.1175/JPO-D-18-0127.1

Zaron, E. D. (2022). Baroclinic tidal cusps from satellite altimetry. *Journal of Physical Oceanography*, *52*(12), 3123–3137. https://doi.org/10.1175/JPO-D-21-0155.1

Zaron, E. D., & Egbert, G. D. (2014). Time-variable refraction of the internal tide at the Hawaiian Ridge. *Journal of Physical Oceanography*, *44*(2), 538–557. https://doi.org/10.1175/JPO-D-12-0238.1

Zilberman, N. V., Merrifield, M. A., Carter, G. S., Luther, D. S., Levine, M. D., & Boyd, T. J. (2011). Incoherent nature of M2 internal tides at the Hawaiian Ridge. *Journal of Physical Oceanography*, *41*(11), 2021–2036. https://doi.org/10.1175/JPO-D-10-05009.1